Article

Chinese Science Bulletin

Materials Science

March 2012 Vol.57 No.8: 935–940
doi: 10.1007/s11434-011-4946-5

Investigation of the electronic structure and photoluminescence properties of Eu^{3+} in $Sr_2Mg_{1-x}Zn_xSi_2O_7$ ($0 \leqslant x \leqslant 1$)

ZHANG ZhiYa* & WANG YuHua

Key Laboratory for Magnetism and Magnetic Materials of the Ministry of Education, Department of Materials Science, School of Physical Science and Technology, Lanzhou University, Lanzhou 730000, China

Received March 23, 2011; accepted October 27, 2011; published online January 11, 2012

Undoped and Eu^{3+}-doped $Sr_2Mg_{1-x}Zn_xSi_2O_7$ ($0 \leqslant x \leqslant 1$) powder crystals were obtained by conventional solid-state reaction. X-ray diffraction, inductively coupled plasma analysis, and Fourier transform infrared spectroscopy results implied that a complete solid-solution formed between $Sr_2MgSi_2O_7$ and $Sr_2ZnSi_2O_7$ as well as local structural adjustment. Excitation spectra exhibited O^{2-}-Eu^{3+} charge transfer (CT) bands centered at 250 nm for $Sr_2MgSi_2O_7$:Eu^{3+} and 258 nm for $Sr_2ZnSi_2O_7$:Eu^{3+}. Emission spectra exhibited a major band around 616 nm, which showed the environment around Eu^{3+} was non-centrosymmetric in both $Sr_2MgSi_2O_7$:Eu^{3+} and $Sr_2ZnSi_2O_7$:Eu^{3+}. In addition, first principles calculations within the local density approximation (LDA) of density functional theory (DFT) were used to calculate the electronic structure of $Sr_2MgSi_2O_7$ and $Sr_2ZnSi_2O_7$. Calculated results were correlated with experimental UV-vis reflection spectra and the observed shift of the O^{2-}-Eu^{3+} CT band.

Zn^{2+}, charge transfer, photoluminescence, local density approximation

Citation: Zhang Z Y, Wang Y H. Investigation of the electronic structure and photoluminescence properties of Eu^{3+} in $Sr_2Mg_{1-x}Zn_xSi_2O_7$ ($0 \leqslant x \leqslant 1$). Chin Sci Bull, 2012, 57: 935–940, doi: 10.1007/s11434-011-4946-5

Zn^{2+} is a typical transition metal ion with $3d^{10}$ electron configuration. Despite the similar ionic radii of Zn^{2+} (74 pm, coordination number (CN) = 4) and Mg^{2+} (71 pm, CN = 4) and their identical valence state, the crystal and/or electronic structure of a material usually changes significantly when substitution occurs between Zn^{2+} and Mg^{2+}. One typical example is Mg_2SiO_4-Zn_2SiO_4:Mg_2SiO_4 possesses an orthorhombic "forsterite" structure while Zn_2SiO_4 belongs to rhombohedral "willemite". Mg^{2+} occupies an octahedral site in Mg_2SiO_4 while Zn^{2+} has tetrahedral coordination in Zn_2SiO_4. The solid solution limits of Zn^{2+} in Mg_2SiO_4 and Mg^{2+} in Zn_2SiO_4 were both observed to be as low as 5 at.% [1]. $MgAl_2O_4$-$ZnAl_2O_4$ is similar; the band gap of $MgAl_2O_4$ is 7.8 eV [2] while that of $ZnAl_2O_4$ is just 3.8–3.9 eV [3]. This implies that Zn^{2+} plays a particular role in crystal and electronic structure changes in these systems. However, further investigation of the role of Zn^{2+} is required. $Sr_2MgSi_2O_7$ and $Sr_2ZnSi_2O_7$ are important hosts for photoluminescent (PL) materials, especially long afterglow phosphors [4–7]. They both possess a tetragonal akermanite-type structure with the space group $P\bar{4}21m$ (SG No. 113) and can form complete solid solutions with each other [8]. In our recent work [9], we found that $Sr_2ZnSi_2O_7$:Mn^{2+} exhibited strong green emission while $Sr_2MgSi_2O_7$:Mn^{2+} was nonemissive upon excitation at both 254 and 147 nm. Because these two materials have similar crystal structures, the different emission properties might result from the different electronic structures of $Sr_2MgSi_2O_7$ and $Sr_2ZnSi_2O_7$. Eu^{3+} has been used as a structural probe because of its particularly sensitive emission [10–12]. In addition, the O^{2-}-Eu^{3+} charge transfer (CT) transition involves both the luminescent center and host, so it can be used to probe the coupling between the luminescent center and host.

In the present work, undoped and Eu^{3+}-doped $Sr_2Mg_{1-x}Zn_xSi_2O_7$ ($0 \leqslant x \leqslant 1$) samples were prepared. Inductively coupled plasma (ICP), Fourier transform infrared (FT-IR),

*Corresponding author (email: zhangzhiya@lzu.edu.cn)

ultraviolet (UV)-visible (vis) diffuse reflection and UV-vacuum UV (VUV) PL spectroscopies as well as X-ray diffraction (XRD) were used to systematically investigate the crystal structure and PL characteristics of the samples. Local density approximation (LDA) calculations within density functional theory (DFT) were employed to estimate the electronic structure as well as the linear optical properties of the samples.

1 Experimental and computational methodology

Undoped and Eu^{3+}-doped (5 at.%) $Sr_2Mg_{1-x}Zn_xSi_2O_7$ ($0 \leqslant x \leqslant 1$) polycrystalline powder samples were prepared by solid-state reaction. $SrCO_3$ (99%, Tianjin No. 3 Chemical Reagent Factory, Tianjin, China), $Mg(NO_3)_2{\cdot}6H_2O$ (99%, Tianjin Yaohua Chemical, Tianjin, China), ZnO (99%, Tianjin No. 3 Chemical Reagent Factory), H_2SiO_3 (99%, Tianjin No. 3 Chemical Reagent Factory), and Eu_2O_3 (99.99%, Beijing Nonferrous Metal Institute, Beijing, China) were used as the starting materials. In Eu^{3+}-doped samples, Eu^{3+} was assumed to replace Sr^{2+} in $Sr_2Mg_{1-x}Zn_xSi_2O_7$ ($0 \leqslant x \leqslant 1$) because of their similar ionic radii. Stoichiometric amounts of the raw materials were weighed and mixed using an agate mortar. The mixture was ground to a fine powder before sintering at 1220°C for 4 h with the heating rate of about 5–7°C/min.

XRD patterns were obtained on a Rigaku D/max-2400 X-ray diffractometer. Excitation and emission spectra were measured using an Edinburgh Instruments FLS920T spectrometer. The scan speed was 30 nm/s with a step of 1 nm and the dwell time was 0.2 s. UV spectra were measured by a steady-state spectrophotometer with a Xe900 xenon arc lamp (450 W) as the excitation source. The slits were 0.18 nm for excitation and 0.8 nm for emission spectra. The VUV light source of the spectrometer system was a 150 W deuterium lamp (Cathodeon Ltd., UK). Emission and excitation spectra were measured using a vacuum monochromator (VM504, Acton Research Co., USA). The slits for the VUV excitation and emission spectra were 0.18 and 2 nm, respectively. FT-IR spectra were obtained on a Thermo Mattson Nicolet Satellite FT-IR spectrophotometer using KBr discs. ICP data were taken with an IRIS Advantage ER/S ICP emission spectrometer (Thermo Jarrell-Ash, USA). UV-VIS diffused reflection spectra were obtained on a LAMBDA 950 spectrometer (Perkin Elmer, USA) using barium sulfate ($BaSO_4$) as a reference.

All of the calculations were based on the LDA of DFT [13,14] using the program CASTEP [15], which is based on planewaves and pseudopotentials. The configuration of $Sr_2MgSi_2O_7$ employed in the calculation was obtained by geometry optimization of the data reported in the literature [16]. The configuration of $Sr_2ZnSi_2O_7$ was obtained by geometry optimization after substitution of the Mg in $Sr_2MgSi_2O_7$ with Zn. The valence electrons considered for Sr, Mg, Zn, Si and O are $4s^24p^65s^2$, $2p^63s^2$, $3d^{10}4s^2$, $3s^23p^2$ and $2s^22p^4$, respectively. The tested rather soft and optimized O pseudopotential in several systems [17–19] enable us to use a kinetic-energy cutoff of 460 eV throughout the calculation. The band gap calculated by LDA is inherently smaller than the experimental result. This error is caused by the discontinuity of the exchange-correlation energy.

2 Results and discussion

All undoped and Eu^{3+}-doped $Sr_2Mg_{1-x}Zn_xSi_2O_7$ ($0 \leqslant x \leqslant 1$) samples appeared as a single phase with tetragonal akermanite-type structure. XRD patterns for $Sr_2Mg_{1-x}Zn_xSi_2O_7$ ($0 \leqslant x \leqslant 1$) with $x = 0$, 0.5 and 1 are shown in Figure 1(a), (b) and (c), respectively. The patterns exhibit similar profiles but the diffraction peaks for the (110) and (001) crystal planes gradually decrease in intensity from $x = 0$ to $x = 0.5$, and disappear when $x > 0.5$. XRD patterns of $Sr_2MgSi_2O_7$ and $Sr_2ZnSi_2O_7$ were simulated using the powder diffraction function of CASTEP; the results are shown in Figure 1(a') and (c'), respectively. The simulated XRD patterns agree well with experimental results. Comparison of Figure 1(a') and (c'), shows that the diffraction peaks marked with "*" including those for the (110) and (001) crystal planes decrease in intensity or disappear in $Sr_2ZnSi_2O_7$. The accordance of the simulated and experimental results confirms the validity of the lattice configuration used in the calculations, which will be discussed further later.

The ICP elemental analysis data in Table 1 and FT-IR spectra in Figure 2 confirm that a complete solid solution forms between $Sr_2MgSi_2O_7$ and $Sr_2ZnSi_2O_7$. Figure 2 shows that the FT-IR spectra of $Sr_2MgSi_2O_7$ and $Sr_2ZnSi_2O_7$ exhibit similar features. Bands at 1005.81, 967.18, 924.13 and 839.13 cm^{-1} for $Sr_2MgSi_2O_7$, and 1006.96, 968.53, 901.16 and 827.81 cm^{-1} for $Sr_2ZnSi_2O_7$ are caused by (Si-O_b-Si)

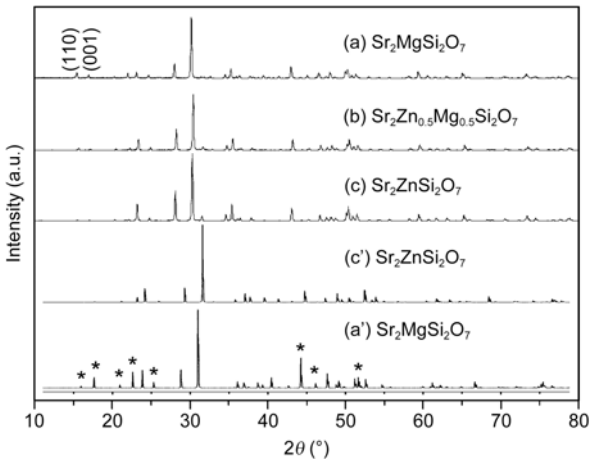

Figure 1 Experimental XRD patterns of $Sr_2Mg_{1-x}Zn_xSi_2O_7$. (a) $x = 0$; (b) $x = 0.5$; (c) $x = 1$. Simulated XRD patterns of $Sr_2Mg_{1-x}Zn_xSi_2O_7$. (a') $x = 0$; (c') $x = 1$.

Table 1 ICP data for $Sr_2Mg_{1-x}Zn_xSi_2O_7$ ($0 \leqslant x \leqslant 1$)

Samples	ICP (%)	
	Mg	Zn
$x=0.00$	–	–
$x=0.25$	76.95	23.05
$x=0.50$	53.72	46.28
$x=0.75$	78.68	21.32
$x=1.00$	–	–

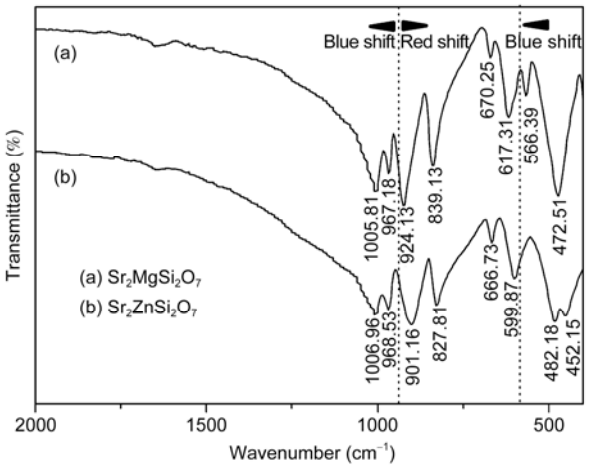

Figure 2 FT-IR spectra of $Sr_2Mg_{1-x}Zn_xSi_2O_7$.

and (Si-O_{nb}) stretching modes [20–23]. Signals at 670.25, 617.31 and 566.39 cm^{-1} for $Sr_2MgSi_2O_7$, and 666.37, 599.87 cm^{-1} for $Sr_2ZnSi_2O_7$ arise from (Si-O-Si) bending [20–23], and those at 472.15 cm^{-1} for $Sr_2MgSi_2O_7$, and 482.18 and 452.15 cm^{-1} for $Sr_2ZnSi_2O_7$ are responsible for the (Si-O-Si) bending modes as well as *M*-O (*M* = Mg, Zn) modes [21,22,24]. In the three areas divided by the dotted lines in Figure 2, the bands from $Sr_2ZnSi_2O_7$ exhibit a red shift in the central area and blue shifts in the other two regions when compared with those of $Sr_2MgSi_2O_7$. In $Sr_2MgSi_2O_7$ and $Sr_2ZnSi_2O_7$, both Mg^{2+} and Zn^{2+} occupy tetrahedral sites [8]. According to Goodenough et al. [25], Zn^{2+} is preferred for tetrahedral sites rather than Mg^{2+} despite the larger radius of Zn^{2+} than Mg^{2+}, and when Zn^{2+} is located in tetrahedral sites, Zn–O bonds are highly covalent in character. In view of this, the substitution of Zn^{2+} for Mg^{2+} should cause the unit cell dimensions or positions of atoms in $Sr_2MgSi_2O_7$ and $Sr_2ZnSi_2O_7$ to differ. Such local structural adjustment should be responsible for the observed changes in the XRD patterns and FT-IR spectra.

Figure 3 shows excitation spectra of $Sr_2Mg_{1-x}Zn_xSi_2O_7$:Eu^{3+} ($0 \leqslant x \leqslant 1$) with $x=0$, 0.5 and 1. The peaks around 250–260 nm are caused by O^{2-}-Eu^{3+} CT transitions and those between 310 and 450 nm arise from Eu^{3+} *f-f* transitions. The O^{2-}-Eu^{3+} CT band shifts to longer wavelength by up to 8 nm

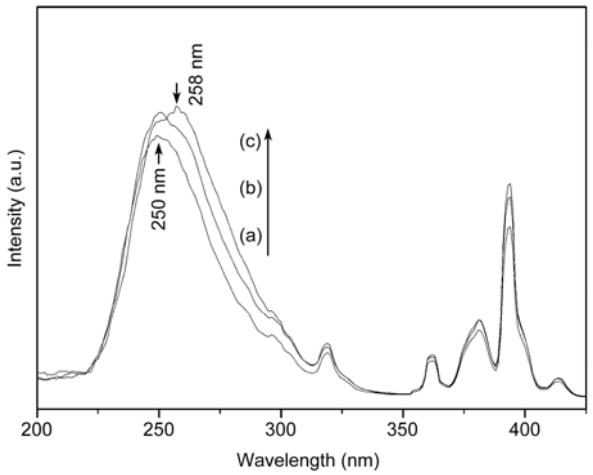

Figure 3 Excitation spectra of $Sr_2Mg_{1-x}Zn_xSi_2O_7$:Eu^{3+}. (a) $x=0$; (b) $x=0.5$; (c) $x=1$. $\lambda_{em}=616$ nm.

and broadens as *x* increases.

To understand the shift of the CT band, it is necessary to consider the electronic structure of $Sr_2MgSi_2O_7$ and $Sr_2ZnSi_2O_7$. As stated previously, the cell parameters of $Sr_2ZnSi_2O_7$ were obtained by optimizing those of $Sr_2MgSi_2O_7$. According to Table 2, the cell parameters of $Sr_2ZnSi_2O_7$ are smaller than those of $Sr_2MgSi_2O_7$, which shows that lattice contraction takes place when Zn substitutes Mg in $Sr_2MgSi_2O_7$. The trend of lattice contraction from $Sr_2MgSi_2O_7$ to $Sr_2ZnSi_2O_7$ is surprising given that Zn has a larger ionic radius than Mg^{2+}. Such contraction can be attributed to the contribution of Zn^{2+} to the electronic structure of $Sr_2ZnSi_2O_7$.

The calculated band structure and density of states (DOS) for the samples are shown in Figures 4 and 5, respectively. In Figure 4(a) and (b), the indirect LDA band gap is 3.95 eV for $Sr_2MgSi_2O_7$ and 3.34 eV for $Sr_2ZnSi_2O_7$. The band gap for $Sr_2MgSi_2O_7$ is slightly smaller than that of 4.2 eV reported for $Ca_2MgSi_2O_7$ [24]. The calculated refractive index *n* is 1.721 and 1.706 for $Sr_2MgSi_2O_7$ and $Sr_2ZnSi_2O_7$, respectively. These values are comparable with 1.720–1.722 for $Ca_2MgSi_2O_7$ [24]. From Figure 4 it can be concluded that: (1) the upper valence band (VB) falls between 0 and −5 eV for $Sr_2MgSi_2O_7$ and possess a wider distribution from 0 to −6.8 eV for $Sr_2ZnSi_2O_7$; (2) the VB top of $Sr_2MgSi_2O_7$ is relatively flat while that of $Sr_2ZnSi_2O_7$ fluctuates. These features are also manifested in the DOS plots presented in Figure 5. Between −10 and 0 eV the DOS exhibit a wider distribution in $Sr_2ZnSi_2O_7$ than in $Sr_2MgSi_2O_7$. Moreover,

Table 2 Optimized lattice parameters of $Sr_2MgSi_2O_7$ and $Sr_2ZnSi_2O_7$

Samples	Cell parameters		
	a (Å)	*b* (Å)	*c* (Å)
$Sr_2MgSi_2O_7$	7.8609	7.8609	5.0290
$Sr_2ZnSi_2O_7$	7.6658	7.6658	5.0107

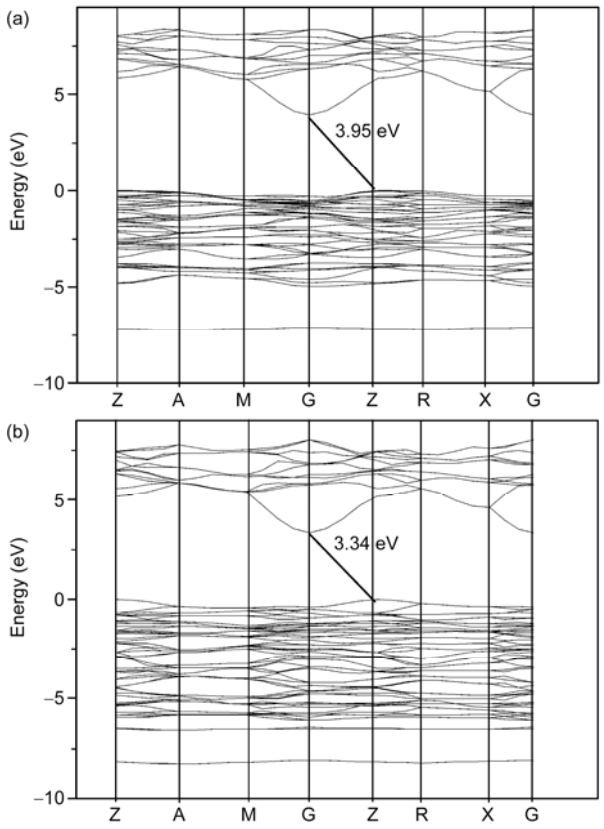

Figure 4 Electronic band structures of (a) $Sr_2MgSi_2O_7$ and (b) $Sr_2ZnSi_2O_7$.

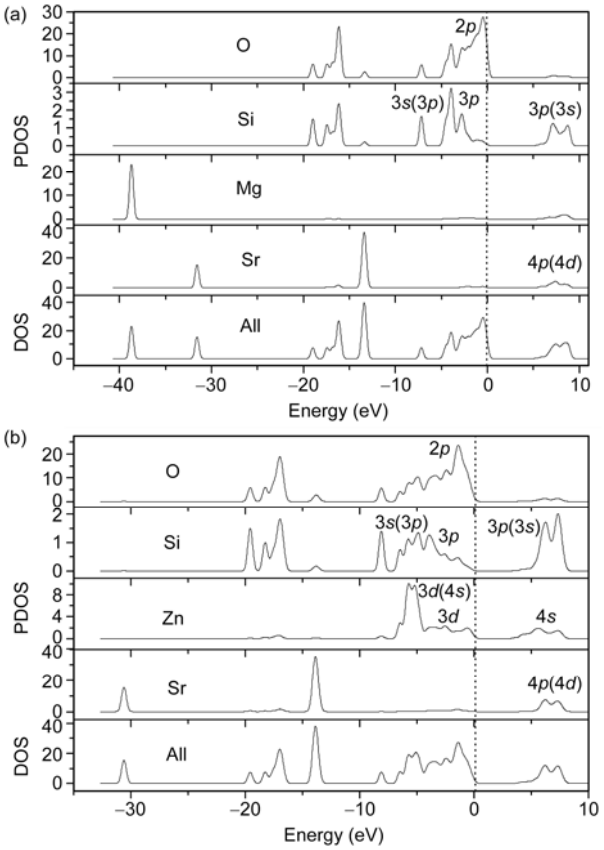

Figure 5 DOS plots of (a) $Sr_2MgSi_2O_7$ and (b) $Sr_2ZnSi_2O_7$.

the Zn 3*d* orbitals hybridize with the coordinating O orbitals and contribute significantly to the upper VB of $Sr_2ZnSi_2O_7$, so Zn–O bonds are mainly covalent. In contrast, Mg has a negligible effect on the VB top of $Sr_2MgSi_2O_7$ and the Mg–O bonds are mainly ionic in character. O(2*p*)-Zn(3*d*) hybridization and its effect on electronic structure has been widely investigated [25–27]. In Ref. [27], it was stated that *p*-*d* repulsion and hybridization lower the band gap and increase the VB offset. As discussed previously, in $Sr_2(Mg,Zn)Si_2O_7$, substitution of Mg with Zn decreases the band gap, broadens the DOS distribution of the upper VB and increases the fluctuation of the VB top. The experimental UV-VIS reflection spectra presented in Figure 6 highlight the difference of the VB top between $Sr_2MgSi_2O_7$ and $Sr_2ZnSi_2O_7$. It is apparent that there is a significant decrease near 392 nm and a plateau at about 370 nm for $Sr_2ZnSi_2O_7$. The inset in Figure 6 shows the theoretical absorption curves for $Sr_2MgSi_2O_7$ and $Sr_2ZnSi_2O_7$. An obvious shoulder is observed for $Sr_2ZnSi_2O_7$.

The above results show that the electrons in the upper VB of $Sr_2ZnSi_2O_7$ are more delocalized with wider energy distribution when compared with those in $Sr_2MgSi_2O_7$. This allows the observed broadening and red shift of the O^{2-}-Eu^{3+} CT band in $Sr_2ZnSi_2O_7$:Eu^{3+} to be explained. The O^{2-}-Eu^{3+} CT transition starts from the top of the VB and ends in the Eu^{2+} ground state [28]. In $Sr_2ZnSi_2O_7$:Eu^{3+}, O(2*p*)-Zn(3*d*) hybridization increases the delocalization of the VB electrons and broadens their energy distribution. Correspondingly, the O^{2-}-Eu^{3+} CT band appears at lower energy and is broader for $Sr_2ZnSi_2O_7$:Eu^{3+} than $Sr_2MgSi_2O_7$:Eu^{3+}.

Figure 7(a) shows typical emission spectra for $Sr_2Mg_{1-x}Zn_xSi_2O_7$:0.05Eu^{3+} ($0 \leqslant x \leqslant 1$) with $x = 0$, 0.5 and 1 following excitation with UV light. The host excitation and emission of $Sr_2MgSi_2O_7$ and $Sr_2ZnSi_2O_7$ are presented in Figure 7(b). Figure 7(a) shows that the emissions are dominated by the Eu^{3+} $^5D_0$-$^7F_2$ electric dipole transition (616 nm), which

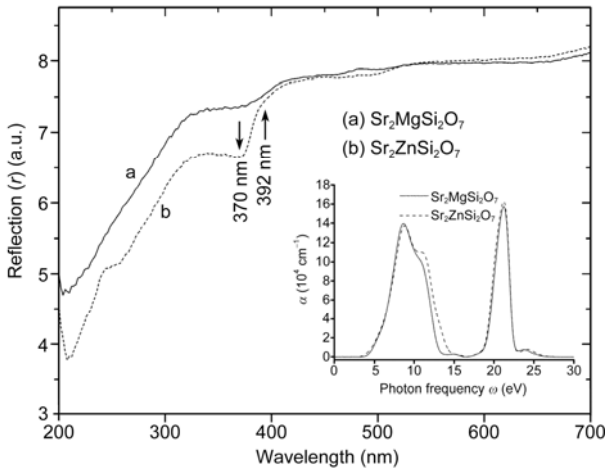

Figure 6 UV-vis diffuse reflection spectra of $Sr_2MgSi_2O_7$ and $Sr_2ZnSi_2O_7$. The inset shows the therotical absorption curves for $Sr_2MgSi_2O_7$ (solid line) and $Sr_2ZnSi_2O_7$ (dotted line).

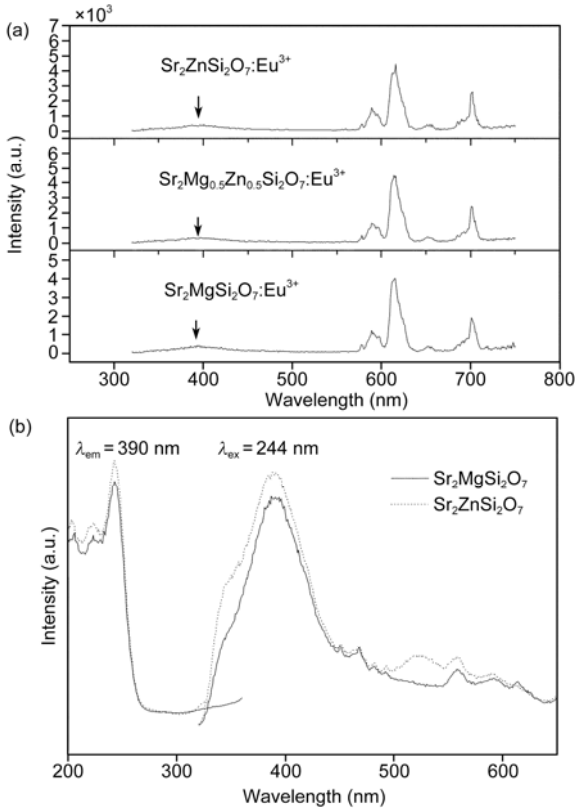

Figure 7 (a) Emission spectra of $Sr_2Mg_{1-x}Zn_xSi_2O_7:Eu^{3+}$ (λ_{ex} = 250–258 nm). (b) Host excitation (λ_{em} = 390 nm) and emission (λ_{ex} = 244 nm) spectra of $Sr_2MgSi_2O_7$ and $Sr_2ZnSi_2O_7$.

indicates that Eu^{3+} occupies non-centrosymmetric sites in $Sr_2(Mg,Zn)Si_2O_7$. Host emission at around 390 nm is also observed in Figure 7(a), which implies that the energy transfer from the host to the activator Eu^{3+} is inefficient despite the considerable overlap between the host emission and Eu^{3+} excitation in $Sr_2Mg_{1-x}Zn_xSi_2O_7:0.05Eu^{3+}$ ($0 \leqslant x \leqslant 1$).

Absorption from the host at around 147 nm was observed for $Sr_2ZnSi_2O_7:Mn^{2+}$ [9], $Sr_2(Mg,Ca)Si_2O_7:Eu^{2+}$ [29] and $Sr_2(Mg,Ca)Si_2O_7:Eu^{2+}$, Dy^{3+} [30]. The theoretical absorption curves for $Sr_2MgSi_2O_7$ and $Sr_2ZnSi_2O_7$ in the inset of Figure 6 exhibit first maxima at about 8.67–8.79 eV (143–141 nm). These experimental and theoretical results suggest that excitation of $Sr_2(Mg,Zn)Si_2O_7$ in the VUV region should be highly efficient. However, the PL spectra show that emission is weak from $Sr_2(Mg,Zn)Si_2O_7:Eu^{3+}$ excited at 147 nm (spectra are not shown here). This is possibly because energy transfer from the host to the activator Eu^{3+} is inefficient in $Sr_2(Mg,Zn)Si_2O_7:Eu^{3+}$.

3 Conclusions

XRD, ICP and FT-IR results showed that a complete solid-solution formed between $Sr_2ZnSi_2O_7$ and $Sr_2MgSi_2O_7$ as well as local structural adjustment. UV excitation spectra exhibited a red shift of up to 8 nm of the O^{2-}-Eu^{3+} CT band from $Sr_2MgSi_2O_7:Eu^{3+}$ to $Sr_2ZnSi_2O_7:Eu^{3+}$, which was related to the effect of Zn^{2+} on the electronic structure of $Sr_2ZnSi_2O_7:Eu^{3+}$ based on experimental UV-VIS reflection spectra and theoretical LDA results. The major emission from $Sr_2Mg_{1-x}Zn_xSi_2O_7:Eu^{3+}$ ($0 \leqslant x \leqslant 1$) following UV excitation was the Eu^{3+} $^5D_0$-$^7F_2$ electric dipole transition around 616 nm, which implies non-inversion symmetry around Eu^{3+}.

This work was supported by the Youth Innovation Research Fund for Interdisciplince of Lanzhou University (*LZUJC200906*) *and the National Natural Science Foundation of China* (*50925206*).

1 Song K X, Chen X M, Zheng C W. Microwave dielectric characteristics of ceramics in Mg_2SiO_4–Zn_2SiO_4 system. Ceram Int, 2008, 34: 917–920
2 Bortz M L, French R H, Jones D J, et al. Temperature dependence of the electronic structure of oxides: MgO, $MgAl_2O_4$ and Al_2O_3. Phys Scr, 1990, 41: 537–541
3 Sampath S K, Cordaro J F. Optical properties of zinc aluminate, zinc gallate, and zinc aluminogallate spinels. J Am Ceram Soc, 1998, 81: 649–654
4 Setlur A A, Srivastava A M, Pham H L, et al. Charge creation, trapping, and long phosphorescence in $Sr_2MgSi_2O_7:Eu^{2+}$, RE^{3+}. J Appl Phys, 2008, 103: 053513
5 Wan J, Yao Y, Tang G, et al. Hydrothermal synthesis and size-enhanced chromaticity of $Sr_2ZnSi_2O_7:Eu^{3+}$ nanoparticles. J Nanosci Nanotechnol, 2008, 8: 1449–1453
6 Yao S, Xue L, Yan Y. Luminescent properties of $Sr_2ZnSi_2O_7:Eu^{2+}$ phosphors prepared by combustion-assisted synthesis method. J Electroceram, 2011, 26: 112–115
7 Hermi F B, Jukka H, Jorma H, et al. Optical energy storage properties of $Sr_2MgSi_2O_7:Eu^{2+}$, R^{3+} persistent luminescence materials. J Therm Anal Calorim, 2011, 105: 657–662
8 Jiang L, Chang C K, Mao D L, et al. Luminescent properties of $Ca_2MgSi_2O_7$ phosphor activated by Eu^{2+}, Dy^{3+} and Nd^{3+}. Opt Mater, 2004, 27: 51–55
9 Hao Y, Wang Y H. Synthesis and photoluminescence of new phosphors $M_2(Mg,Zn)Si_2O_7:Mn^{2+}$ (M = Ca, Sr, Ba). Mater Res Bull, 2007, 42: 2219–2223
10 Yang H C, Li C Y, He H, et al. VUV–UV excited luminescent properties of $LnCa_4O(BO_3)_3:RE^{3+}$ (Ln = Y, La, Gd; Re = Eu, Tb, Dy, Ce). J Lumin, 2006, 118: 61–69
11 Diogo P V, Ieda L V R, Elaine C P, et al. The role of the Eu^{3+} ions in structure and photoluminescence properties of $SrBi_2Nb_2O_9$ powders. Opt Mater, 2009, 31: 995–999
12 Dong Q, Wang Y, Wang Z, et al. Self-purification-dependent unique photoluminescence properties of $YBO_3:Eu^{3+}$ nanophosphors under VUV excitation. J Phys Chem C, 2010, 114: 9245–9249
13 Hohenberg P, Kohn W. Inhomogeneous electron gas. Phys Rev, 1964, 136: B864–B871
14 Kohn W, Sham L J. Self-consistent equations including exchange and correlation effects. Phys Rev, 1965, 140: A1133–A1138
15 CASTEP Program. Version 3.5. San Diego, CA: Molecular Simulations Inc., 1997
16 Kimata M. The structural properties of synthetic Sr-åkermanite, $Sr_2MgSi_2O_7$. Z Kristallogr, 1983, 163: 295–304
17 Takada A, Catlow C R A, Lin J S, et al. *Ab initio* total-energy pseudopotential calculations for polymorphic B_2O_3 crystals. Phys Rev B, 1995, 51: 1447–1455
18 Dawson I, Bristowe P D, Lee M H, et al. First-principles study of a tilt grain boundary in rutile. Phys Rev B, 1996, 54: 13727–13733
19 Lee M H, Cheng C F, Heine V, et al. Distribution of tetrahedral and

octahedral A1 sites in gamma alumina. Chem Phys Lett, 1997, 265: 673–676
20 Frost R L, Bouzaid J M, Reddy B J. Vibrational spectroscopy of the sorosilicate mineral hemimorphite $Zn_4(OH)_2Si_2O_7·H_2O$. Polyhedron, 2007, 26: 2405–2412
21 Chandrappa G T, Ghosh S, Patil K C. Synthesis and properties of willemite, Zn_2SiO_4, and M^{2+}:Zn_2SiO_4 (M = Co and Ni). J Mater Syn Process, 1999, 7: 273–279
22 Makreski P, Jovanovski G, Kaitner B, et al. Minerals from Macedonia: XVIII. Vibrational spectra of some sorosilicates. Vib Spectrosc, 2007, 44: 162–170
23 Abo-Naf S M, El Batal F H, Azooz M A. Characterization of some glasses in the system SiO_2, Na_2O·RO by infrared spectroscopy. Mater Chem Phys, 2002, 77: 846–852
24 Caracas R, Gonze X. *Ab initio* determination of the ground-state properties of $Ca_2MgSi_2O_7$ åkermanite. Phys Rev B, 2003, 68: 84102
25 Goodenough J B, Loeb A L. Theory of ionic ordering, crystal distortion, and magnetic exchange due to covalent forces in spinels. Phys Rev, 1955, 98: 391–408
26 Göpel W, Pollmann J, Ivanov I, et al. Angle-resolved photoemission from polar and nonpolar zinc oxide surfaces. Phys Rev B, 1982, 26: 3144–3150
27 Wei S H, Zunger A. Role of metal *d* states in II-VI semiconductors. Phys Rev B, 1988, 37: 8958–8981
28 Li L, Zhang S. Dependence of charge transfer energy on crystal structure and composition in Eu^{3+}-doped compounds. J Phys Chem B, 2006, 110: 21438–21443
29 Chen Y, Liu B, Kirm M, et al. Luminescent properties of blue-emitting long afterglow phosphors $Sr_{2-x}Ca_x$ $MgSi_2O_7$:Eu^{2+}, Dy^{3+} (x = 0, 1). J Lumin, 2006, 118: 70–78
30 Li Y Z, Wang Y H, Zhang Z H, et al. Precipitation synthesis of $Sr_2MgSi_2O_7$:Eu^{2+} phosphor and its luminescent properties under vacuum ultraviolet excitation. Electrochem Solid-State Lett, 2006, 9: J37–J39